Supporting Information for "Understanding Contributions of Paleo-Informed Natural Variability and Climate Changes on Hydroclimate Extremes in the Central Valley Region of California"

Rohini S. Gupta[1], Scott Steinschneider[2], Patrick M. Reed[1]

[1]School of Civil and Environmental Engineering, Cornell University, Ithaca, NY, USA

[2]Department of Biological and Environmental Engineering, Cornell University, Ithaca, NY, USA

Contents

1. Table S1
2. Text S1
3. Figures S1-S22, Text S2

Tables

Basin	Area (acre-ft)	Elevation (ft)	Slope
Tuolumne	3983	1795	12.6409
Millerton	4338	2156	13.0847
Merced	2784	1647	13.4917
New Hogan Lake	940	639	9.0975
New Melones	2331	1735	12.4246

Table S1. Physical attributes of the five basins as summarized in Wi and Steinschneider (2022).

Corresponding author: R.S. Gupta, rg727@cornell.edu

Text S1: Fitting the Paleo-Conditioned Non-Homogeneous Hidden Markov Model

We fit a Non-Homogeneous Hidden Markov Model (NHMM) in order to generate ensembles of plausible daily traces of weather regimes through the 600-year reconstruction. As compared to a Hidden Markov Model which has a stationary transition probability matrix, the NHMM has dynamic transition probability matrices that are conditioned on one or more external covariates that influence transitions between states. In this case, the covariates are the products of the reconstruction which are the first four principal components of weather regime occurrence. More information on the principal components can be found in Gupta et al. (2022). The NHMM is first fit over the instrumental period to the first nine principal components of daily, 500 hPa geopotential height from NOAA-CIRES-DOE Twentieth Century Reanalysis (V3) dataset (Slivinski et al., 2019) between 180-100°W and 30-60°N (i.e., the Pacific/North American sector) from 1950-2017 using the depmixS4 package in R. It is conditioned with the four reconstructed principal components (PC_{WR} from the Gupta et al. (2022) reconstruction) that overlap the same time period. The result from this fitting a time-varying transition probability matrix shown in Equation 1:

$$P(WR_t = i | WR_t = j, X_t = x) = \frac{\exp(\beta_{0j,i} + \beta'_{j,i})}{\sum_{k=1}^{K} \exp(\beta_{0j,i} + \beta'_{j,i})} \tag{1}$$

Here, the transition probability from WR i to WR j at time t is conditioned on $X'_t = [PC_{WR_{1,t}}, PC_{WR_{2,t}}, PC_{WR_{3,t}}, PC_{WR_{4,t}}]$ a vector of daily covariates developed by repeating the annual values of each for each day of the year. These covariates (Level 1 in Figure 3) are used within a multinomial logistic regression with intercepts $\beta_{0j,i}$ and coefficients $\beta_{j,i}$ to define the transition probabilities, with a prime denoting the vector transpose.

Table S2. NHMM Transition Matrix

	WR 1	WR 2	WR 3	WR 4	WR 5
WR 1	$P(1\|1) = \beta_{0,1\|1} + \sum_{k=1}^{4} \beta_{k,1\|1} * PC_{WR_k}$	$P(1\|2) = \beta_{0,1\|2} + \sum_{k=1}^{4} \beta_{k,1\|2} * PC_{WR_k}$	$P(1\|3) = \beta_{0,1\|3} + \sum_{k=1}^{4} \beta_{k,1\|3} * PC_{WR_k}$	$P(1\|4) = \beta_{0,1\|4} + \sum_{k=1}^{4} \beta_{k,1\|4} * PC_{WR_k}$	$P(1\|5) = \beta_{0,1\|5} + \sum_{k=1}^{4} \beta_{k,1\|5} * PC_{WR_k}$
WR 2	$P(2\|1) = \beta_{0,2\|1} + \sum_{k=1}^{4} \beta_{k,2\|1} * PC_{WR_k}$	$P(2\|2) = \beta_{0,2\|2} + \sum_{k=1}^{4} \beta_{k,2\|2} * PC_{WR_k}$	$P(2\|3) = \beta_{0,2\|3} + \sum_{k=1}^{4} \beta_{k,2\|3} * PC_{WR_k}$	$P(2\|4) = \beta_{0,2\|4} + \sum_{k=1}^{4} \beta_{k,2\|4} * PC_{WR_k}$	$P(2\|5) = \beta_{0,2\|5} + \sum_{k=1}^{4} \beta_{k,2\|5} * PC_{WR_k}$
WR 3	$P(3\|1) = \beta_{0,2\|1} + \sum_{k=1}^{4} \beta_{k,3\|1} * PC_{WR_k}$	$P(3\|2) = \beta_{0,3\|2} + \sum_{k=1}^{4} \beta_{k,3\|2} * PC_{WR_k}$	$P(3\|3) = \beta_{0,3\|3} + \sum_{k=1}^{4} \beta_{k,3\|3} * PC_{WR_k}$	$P(3\|4) = \beta_{0,3\|4} + \sum_{k=1}^{4} \beta_{k,3\|4} * PC_{WR_k}$	$P(3\|5) = \beta_{0,3\|5} + \sum_{k=1}^{4} \beta_{k,3\|5} * PC_{WR_k}$
WR 4	$P(4\|1) = \beta_{0,4\|1} + \sum_{k=1}^{4} \beta_{k,4\|1} * PC_{WR_k}$	$P(4\|2) = \beta_{0,4\|2} + \sum_{k=1}^{4} \beta_{k,4\|2} * PC_{WR_k}$	$P(4\|3) = \beta_{0,4\|3} + \sum_{k=1}^{4} \beta_{k,4\|3} * PC_{WR_k}$	$P(4\|4) = \beta_{0,4\|4} + \sum_{k=1}^{4} \beta_{k,4\|4} * PC_{WR_k}$	$P(4\|5) = \beta_{0,4\|5} + \sum_{k=1}^{4} \beta_{k,4\|5} * PC_{WR_k}$
WR 4	$P(5\|1) = \beta_{0,5\|1} + \sum_{k=1}^{4} \beta_{k,5\|1} * PC_{WR_k}$	$P(5\|2) = \beta_{0,5\|2} + \sum_{k=1}^{4} \beta_{k,5\|2} * PC_{WR_k}$	$P(5\|3) = \beta_{0,5\|3} + \sum_{k=1}^{4} \beta_{k,5\|3} * PC_{WR_k}$	$P(5\|4) = \beta_{0,5\|4} + \sum_{k=1}^{4} \beta_{k,5\|4} * PC_{WR_k}$	$P(5\|5) = \beta_{0,5\|5} + \sum_{k=1}^{4} \beta_{k,5\|5} * PC_{WR_k}$

Table S2 shows this symbolic transition matrix. The coefficients of the regression are fit during the instrumental period, and the matrix can vary depending on the value of the daily PC_{WR} from the reconstruction. Thus, a different transition matrix can be developed for each day. From this sequence of daily transition matrices, plausible sequences of daily WRs can be simulated across the entire 600-year period.

Figures

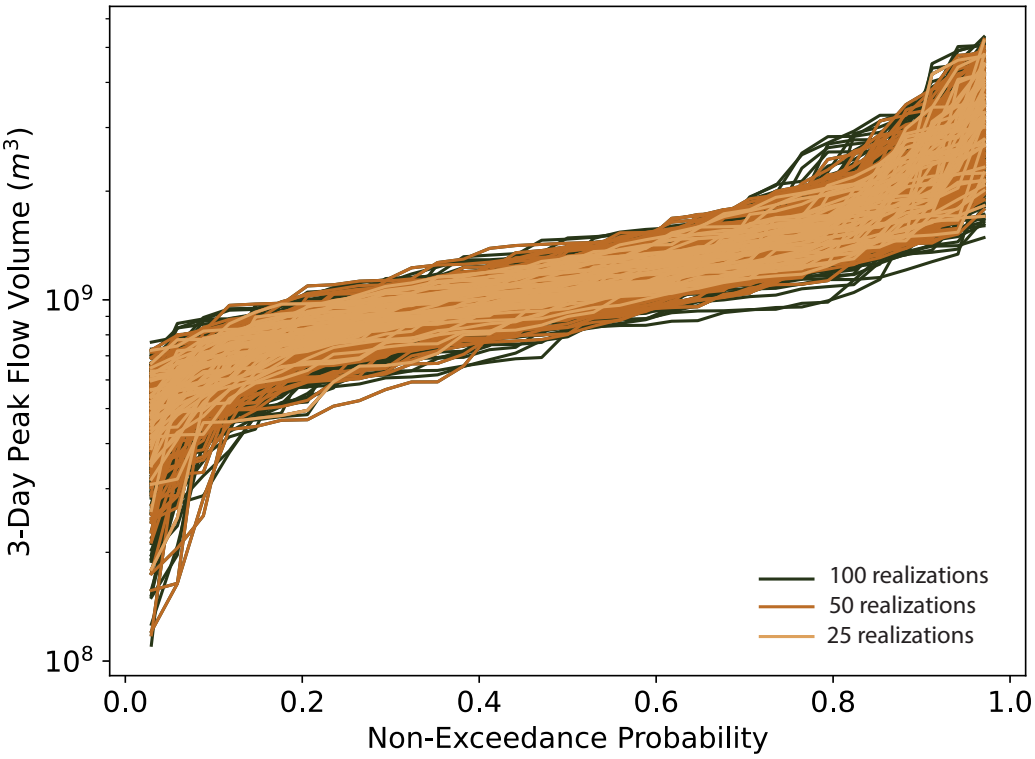

Figure S1. Flow duration curves of 3-day peak flow corresponding to different ensemble sizes. Each line corresponds to 30-year chunks of the 600-year record.

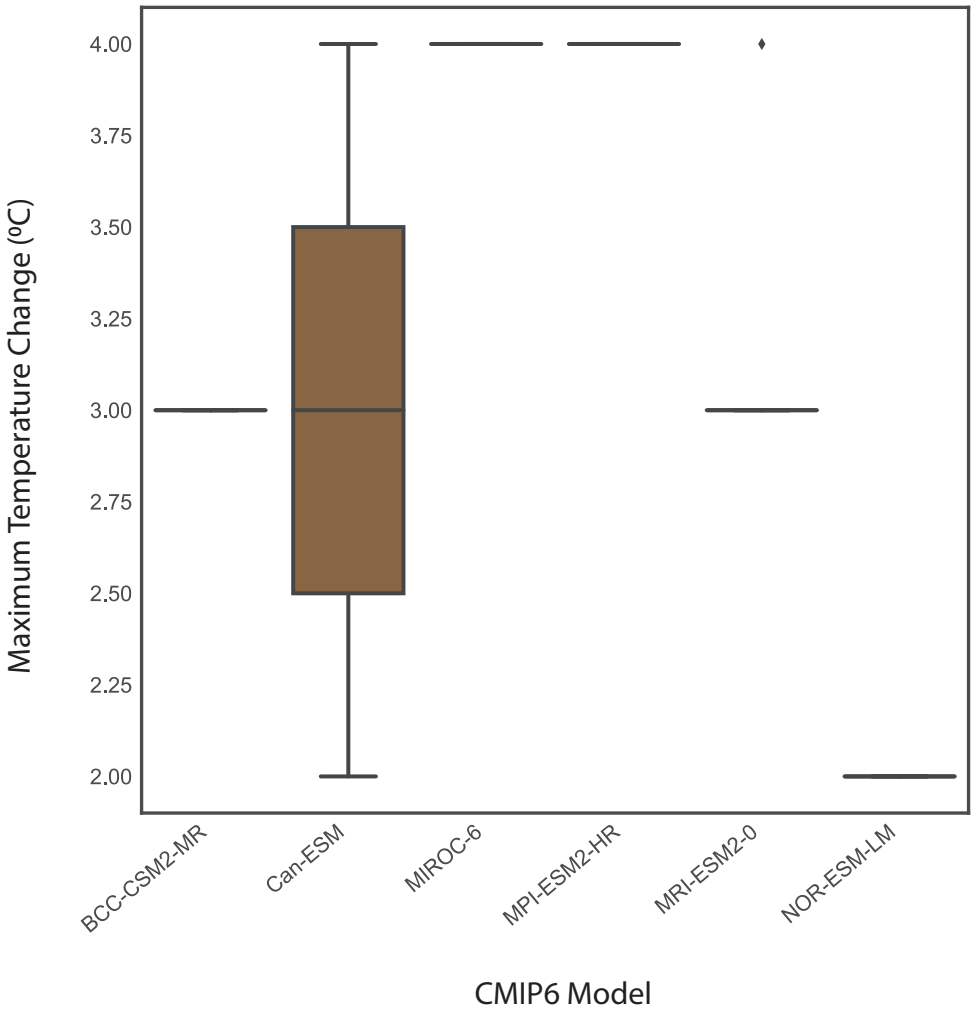

Figure S2. Maximum temperature change dictated by the subset of CMIP6 models downscaled by CarbonPlan (Chegwidden et al., 2022) and for the length of the projection from 2015-2050. All models are run under one initial condition and under multiple downscaling methods.

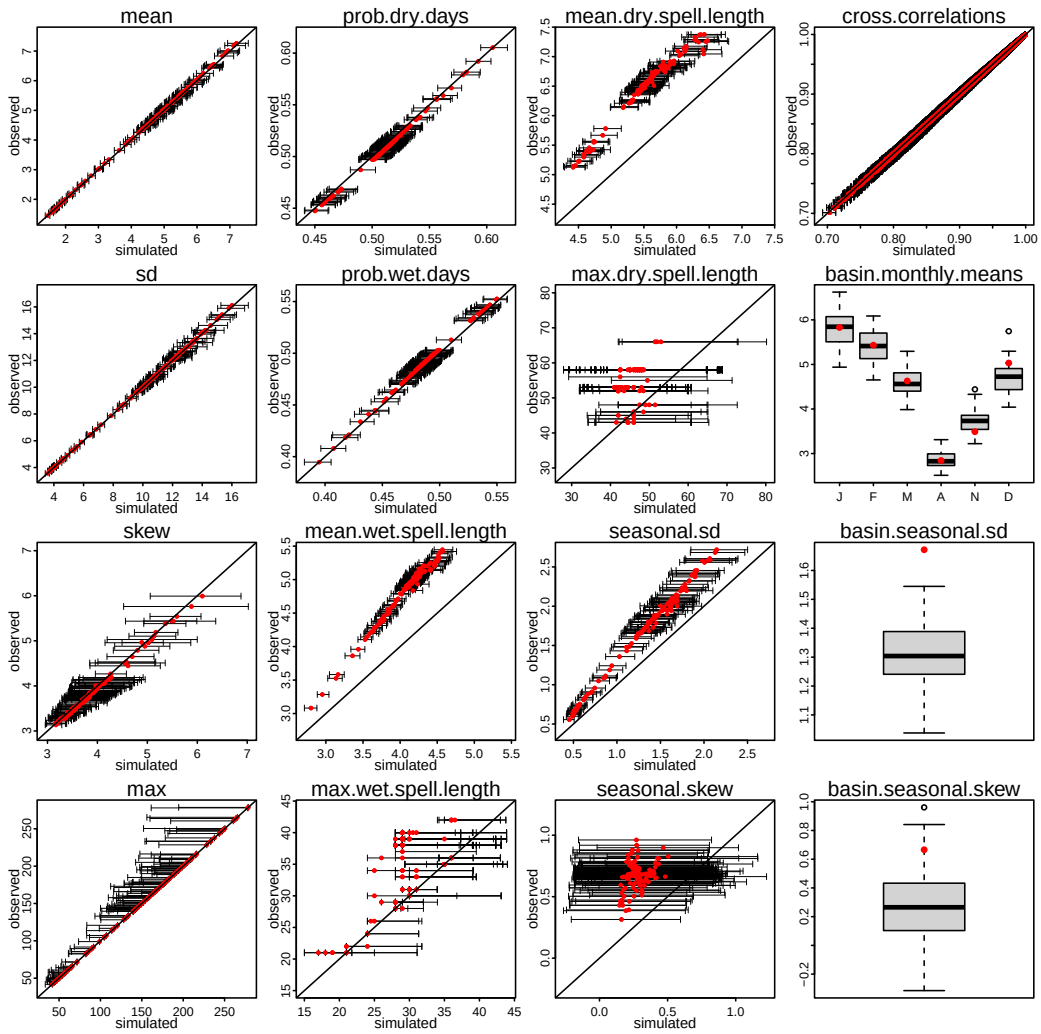

Figure S3. Observed vs. simulated characteristics of daily precipitation in the Tuolumne Basin. For at-site characteristics (180 grid cells), the 95% range for simulated statistics across the 50 ensemble members is shown with whiskers. For basin-averaged statistics, the distribution of simulated statistics is shown as a boxplot along with the observed value.

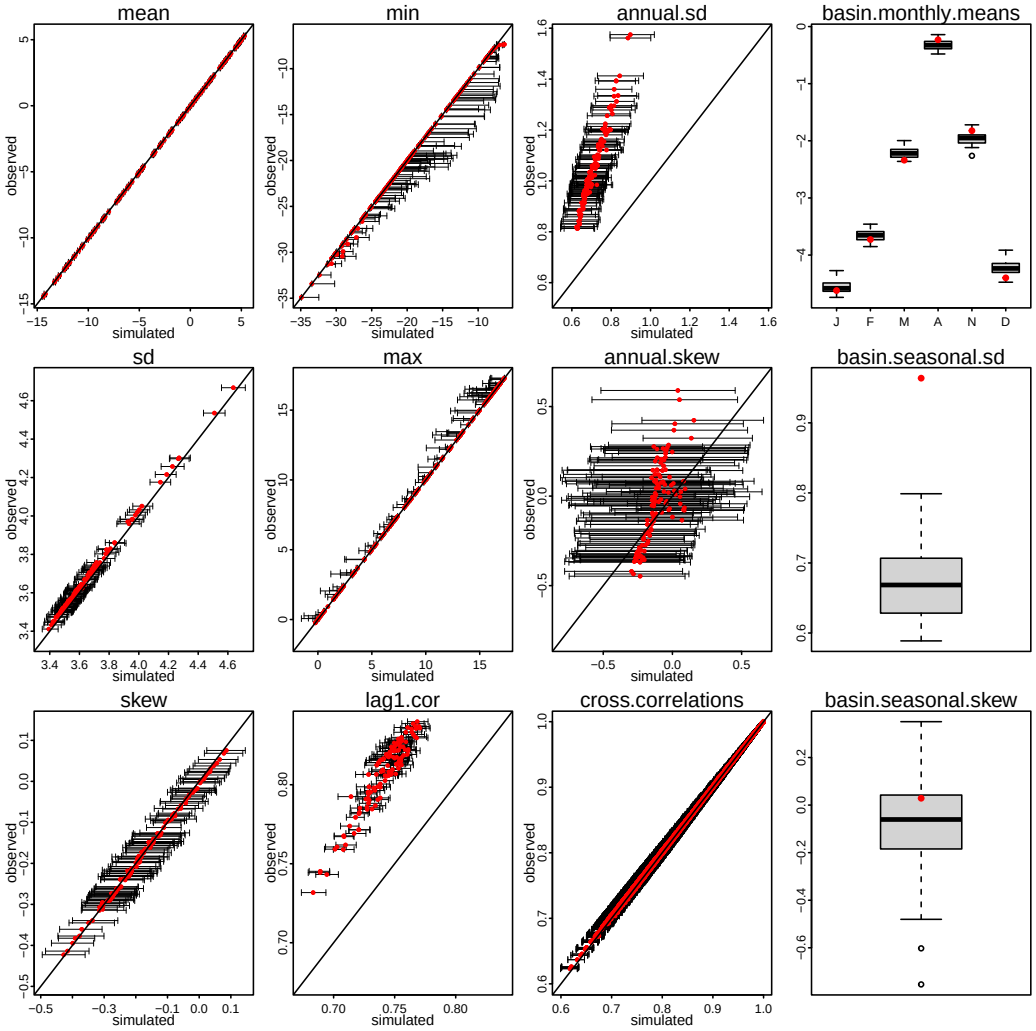

Figure S4. Same as Figure S3 but for observed vs. simulated characteristics of minimum daily temperature in the Tuolumne Basin.

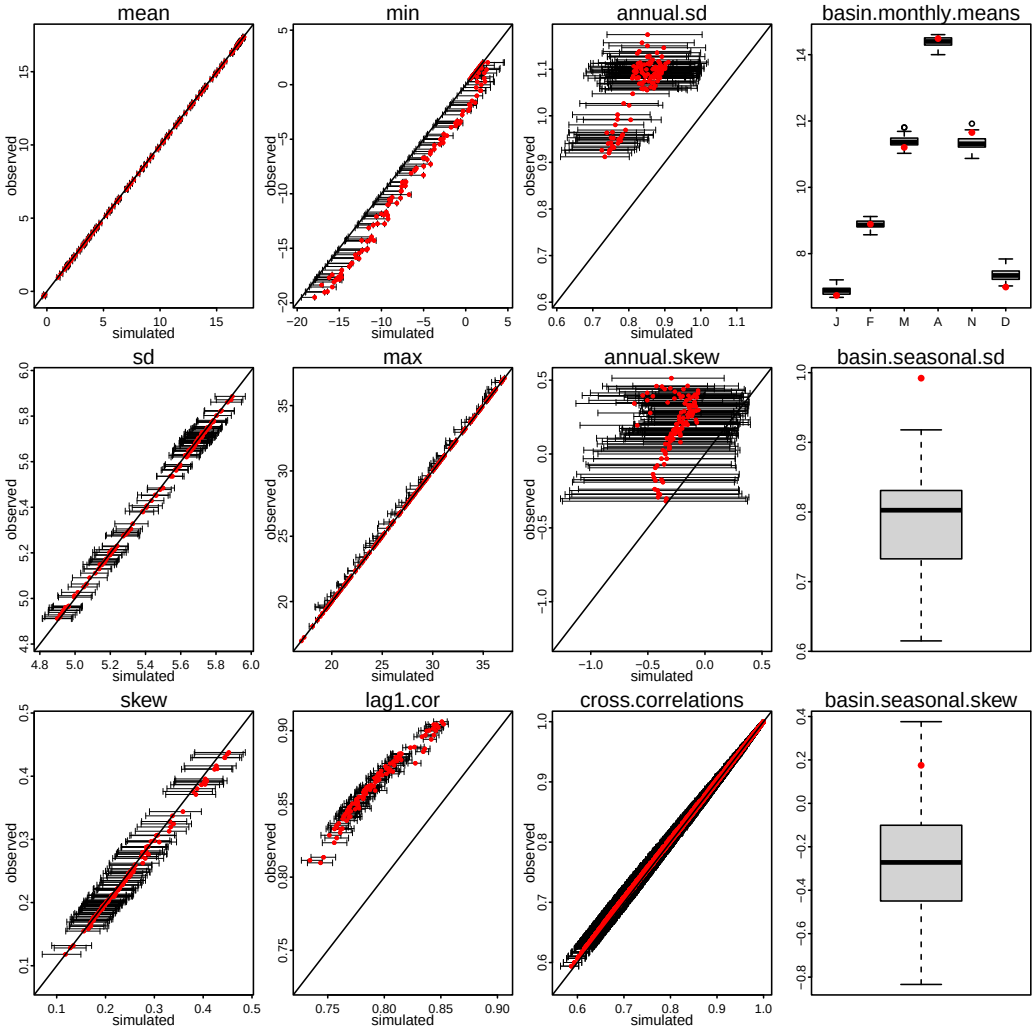

Figure S5. Same as Figure S3 but for observed vs. simulated characteristics of maximum daily temperature in the Tuolumne Basin.

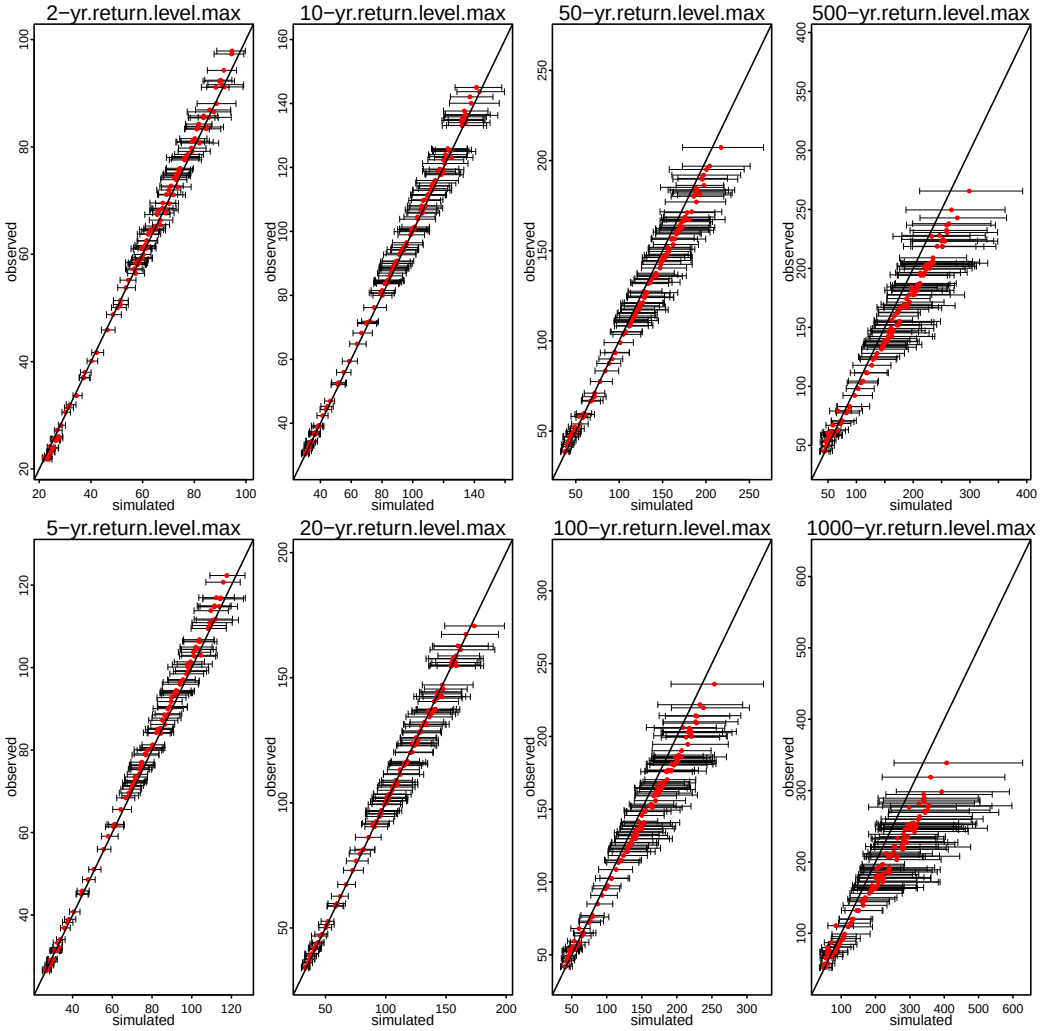

Figure S6. Same as Figure S3 but for observed vs. simulated characteristics of flooding return levels.

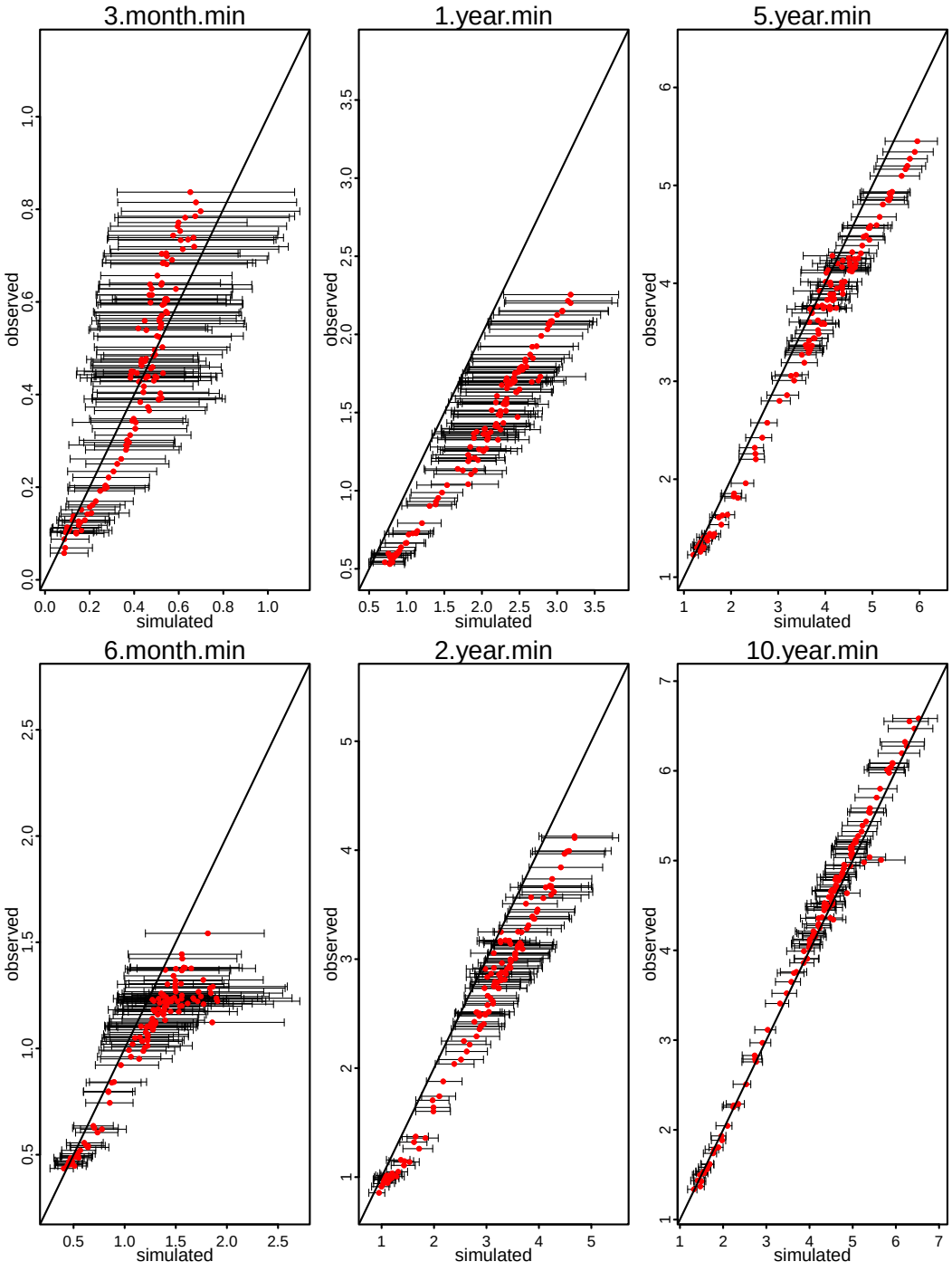

Figure S7. Same as Figure S1 but for observed vs. simulated characteristics of accumulated minimum precipitation totals across varying time periods.

Text S2: Distinctions Across Hydrologic Models

Streamflow ensembles are developed using two hydrologic models: SAC-SMA and HYMOD. Figure S8 shows exceedance plots of 3-day flows associated with each model with a focus on the Don Pedro gauge in the Tuolumne Basin. The flow duration curves exhibit strong differences. The models capture similar peak flow dynamics, but have strong lower-tail distinctions. Particularly, SAC-SMA is capable of producing drier three-day flows. We further conduct a small variance decomposition experiment using SAC-SMA and HYMOD in the Tuolumne Basin. Figures S21 and S22 show the results of the decomposition when choice of hydrologic model is an additional uncertain factor for the flood and drought metrics respectively. Overall, we demonstrate that the choice of model does not impact key drivers of the metrics of interest. Wi and Steinschneider (2022) also demonstrate better out-of-sample performance of SAC-SMA in all five basins over the observed record. Due to these reasons, we opt to continue the study with a single model and choose SAC-SMA.

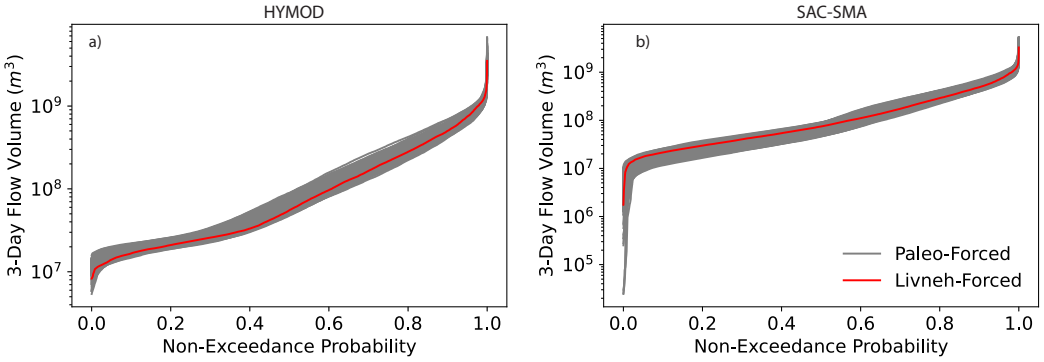

Figure S8. Non-exceedance plots of 3-day flow volumes associated with each model for the Tuolumne Basin. Each grey line represents sorted volumes for each year in 30-year chunks of the paleo-reconstruction across all 50 ensemble members. The red line corresponds to sorted volumes for the 30-year modern record as derived from forcing SAC-SMA-with historic Livneh data from 1987-2013.

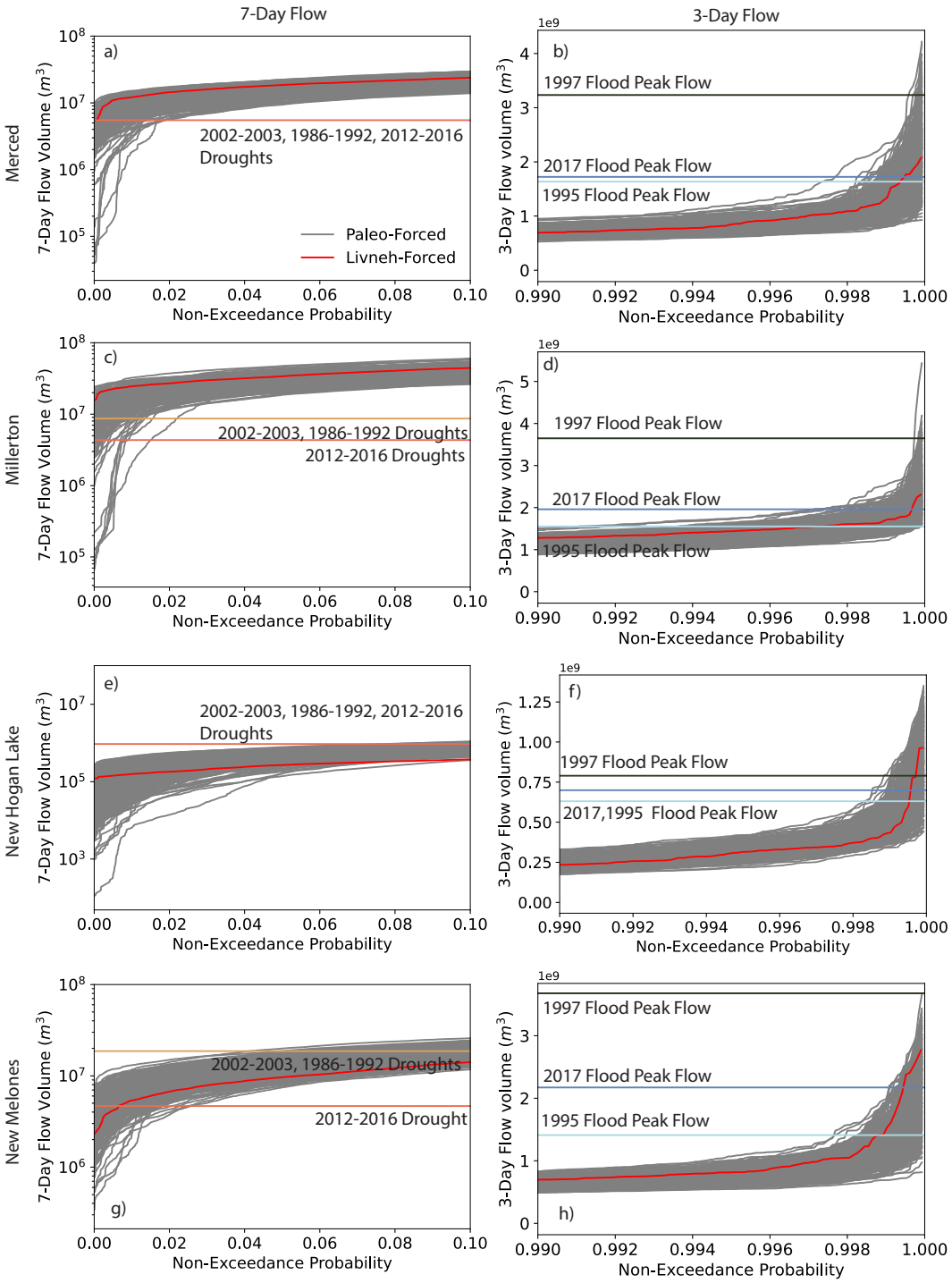

Figure S9. 7-day and 3-day flow volumes at gauged locations across the five basins derived from the paleo-informed streamflow ensembles compared to the Livneh-forced generator over the modern period. Key events from the observed record are shown as colored lines. Each grey line represents sorted volumes for each year in 30-year chunks of the paleo-reconstruction across all 50 ensemble members.

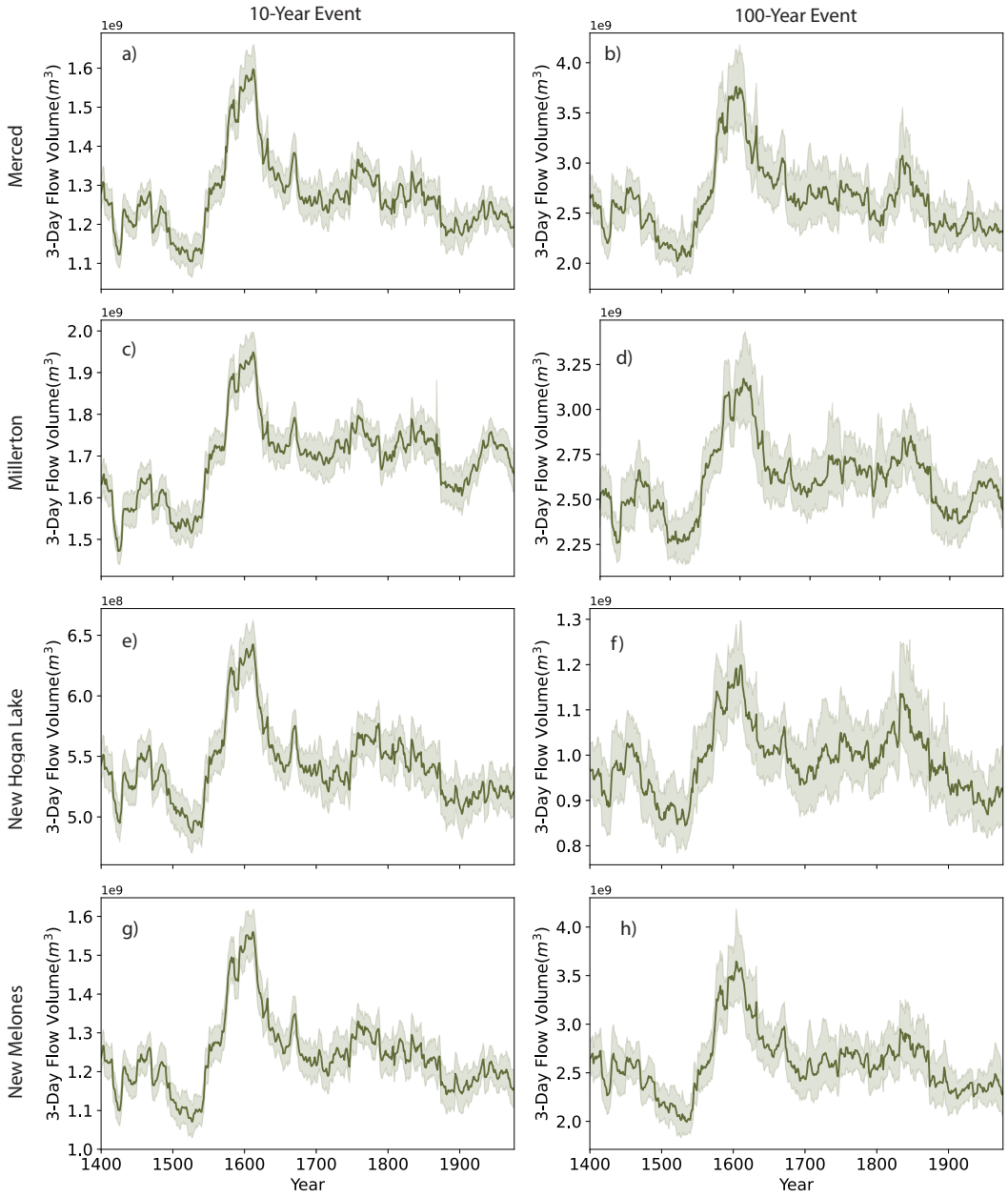

Figure S10. Three-day annual maxima associated with the 10-year return period event and 100-year return period event for remaining four gauged locations. calculated in 30-year moving windows and across the time period from 1400-2017. The dark green line represents the mean flooding return levels and the shading represents the 5^{th} and 95^{th} percentile bounds.

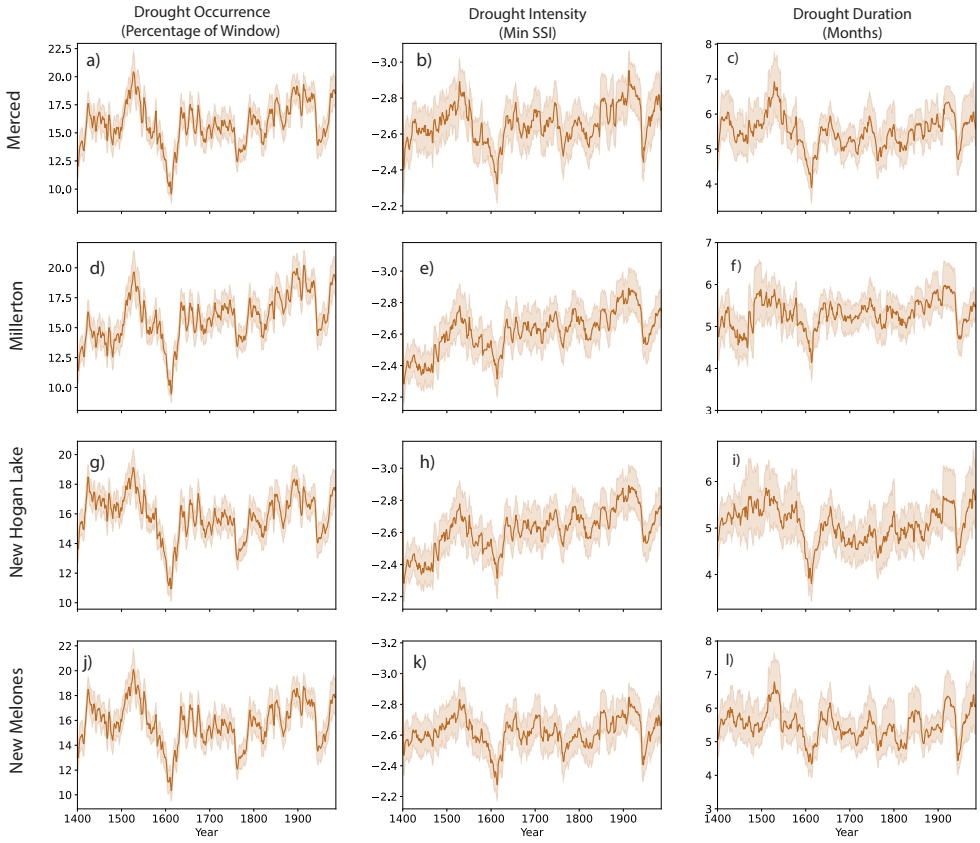

Figure S11. SSI-based hydrologic drought metrics for the remaining four locations calculated in 30-year moving windows and across the time period from 1400-2017. The dark tan line represents the mean drought metric value and the shading represents the 5^{th} and 95^{th} percentile bounds.

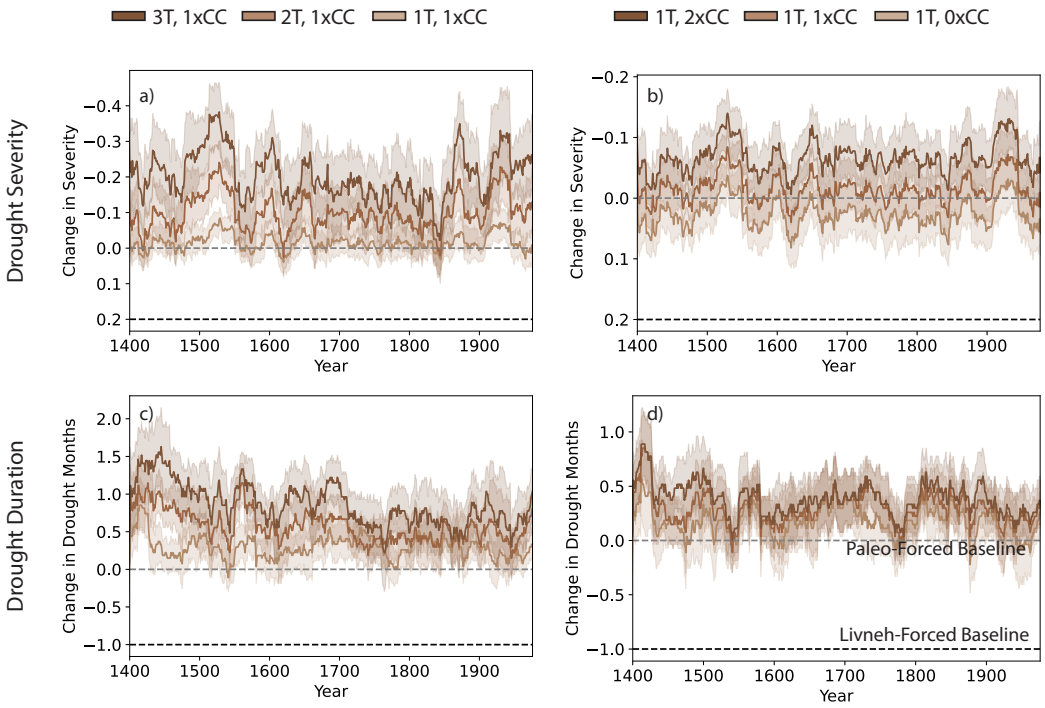

Figure S12. The effect of increasing a,c) temperature and b,d) precipitation scaling rates on drought severity a,b) and drought duration c,d) at Don Pedro (Tuolumne Basin). The dark brown lines represent the increase in the percentage of the 30-year window classified in drought conditions with respect to the baseline scenario (gray dashed line at 0) and the shading represents the 5^{th} and 95^{th} percentile bounds.. A modern baseline (black line) is included as reference and represents the distance from the modern metric to the worst drought duration or severity recorded in the reconstruction.

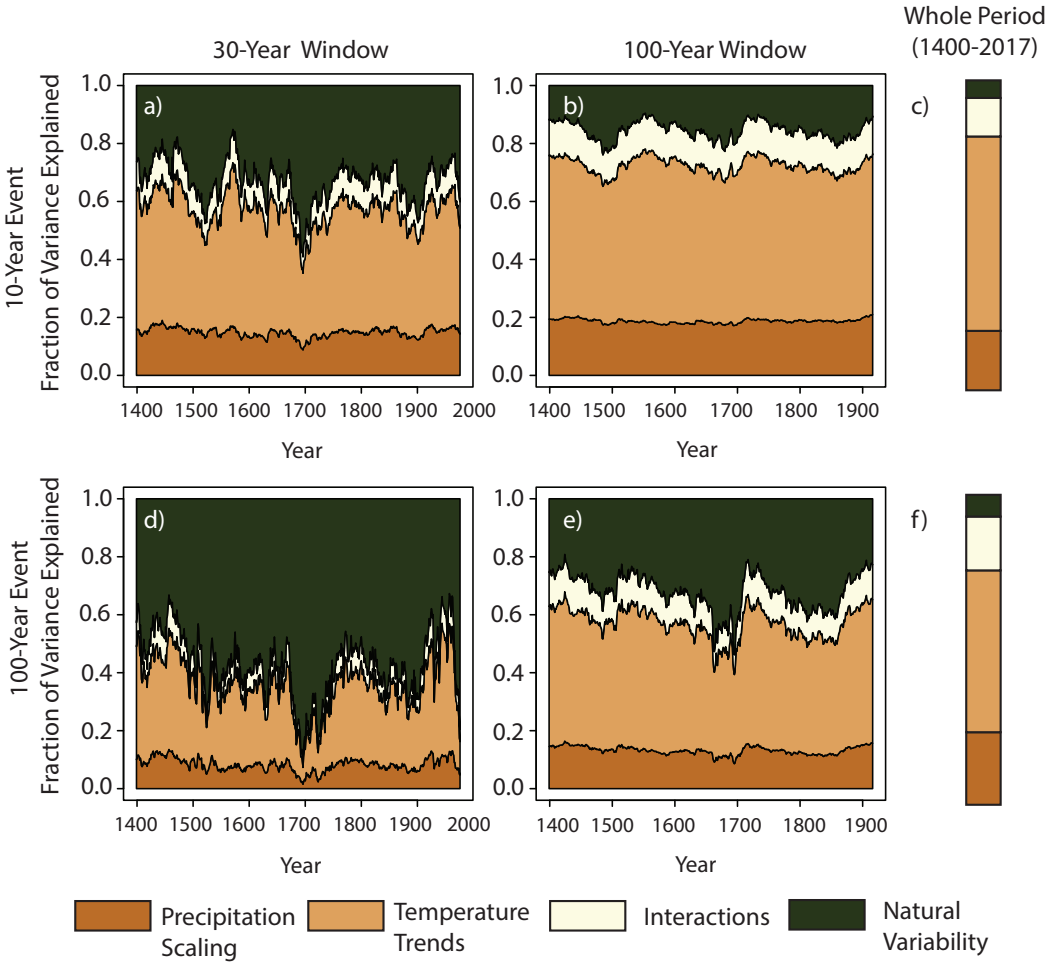

Figure S13. A decomposition of the key drivers of variance in the flood metrics for the Merced Falls gauge in the Merced River Basin for an a,d) 30-year window b,e) 100-year window and c,f) a 600-year window.

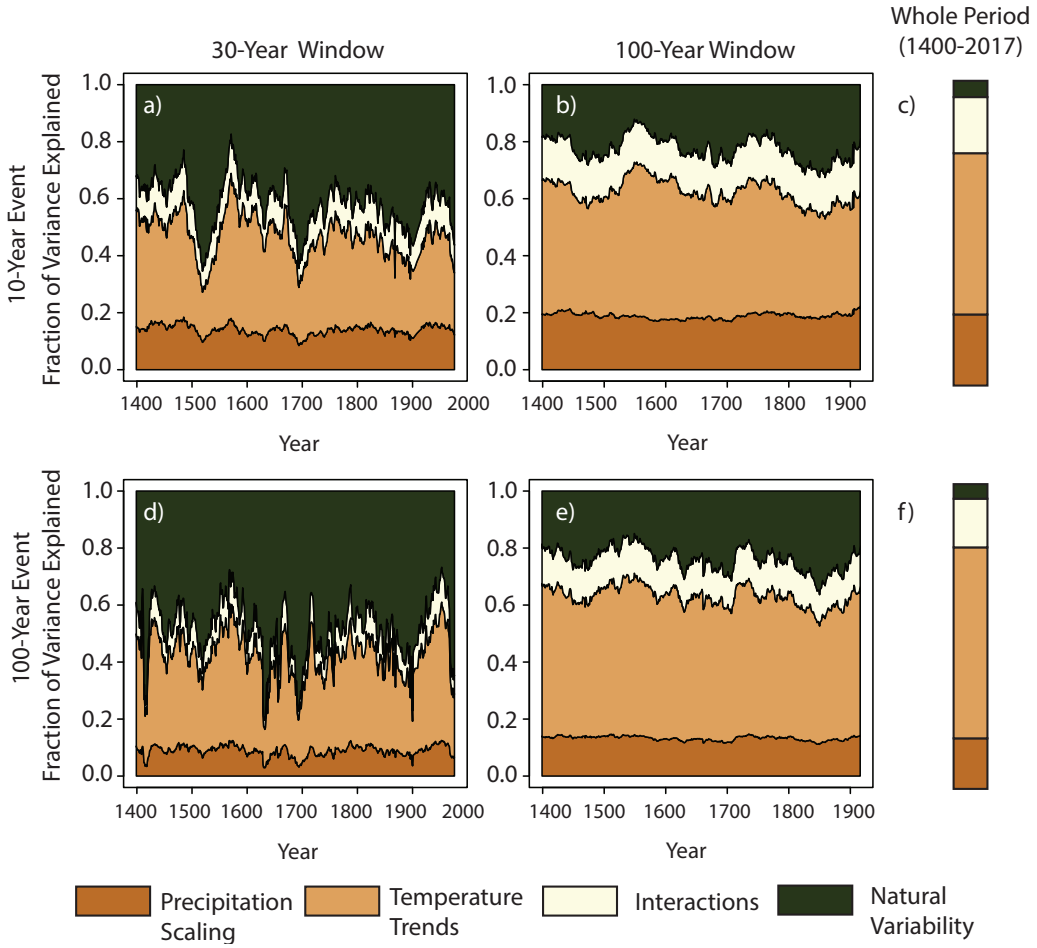

Figure S14. A decomposition of the key drivers of variance in the flood metrics for the Millerton Lake gauge in the San Joaquin Basin for an a,d) 30-year window b,e) 100-year window and c,f) a 600-year window.

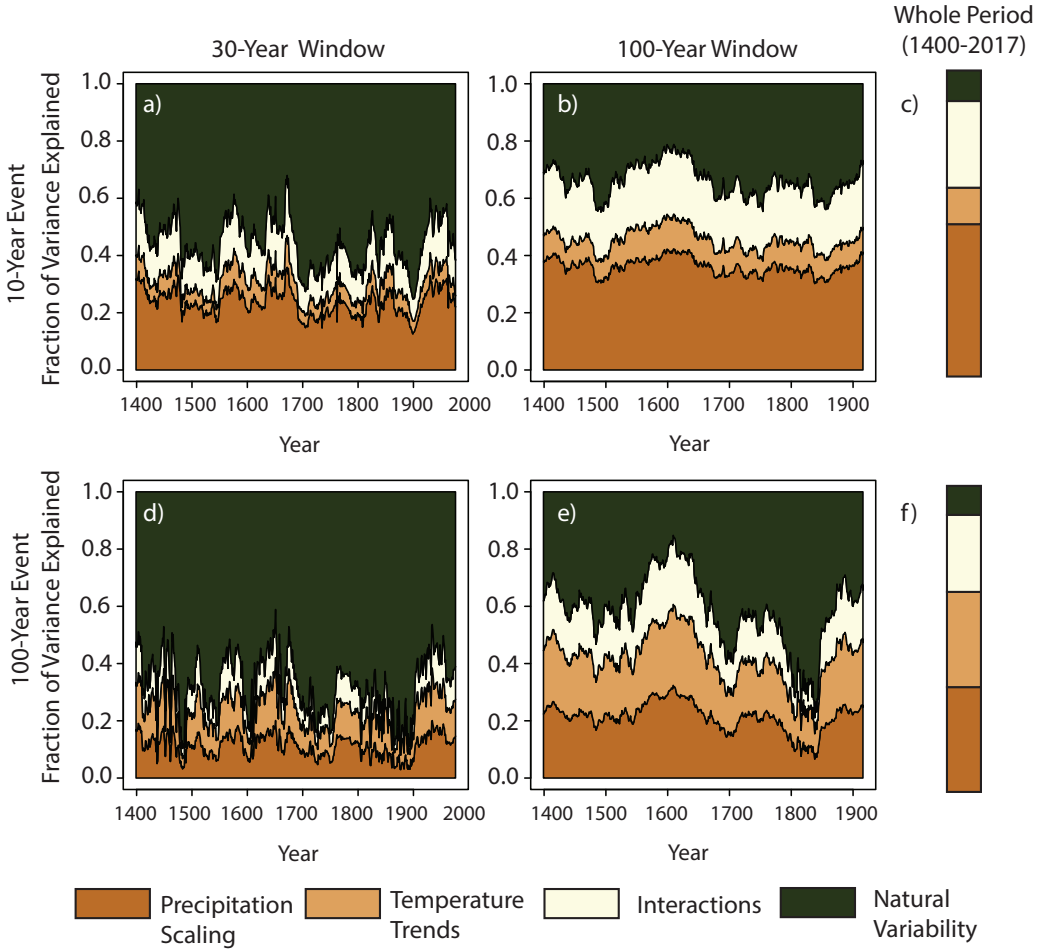

Figure S15. A decomposition of the key drivers of variance in the flood metrics for the New Hogan Lake gauge in the Calaveras River Basin for an a,d) 30-year window b,e) 100-year window and c,f) a 600-year window.

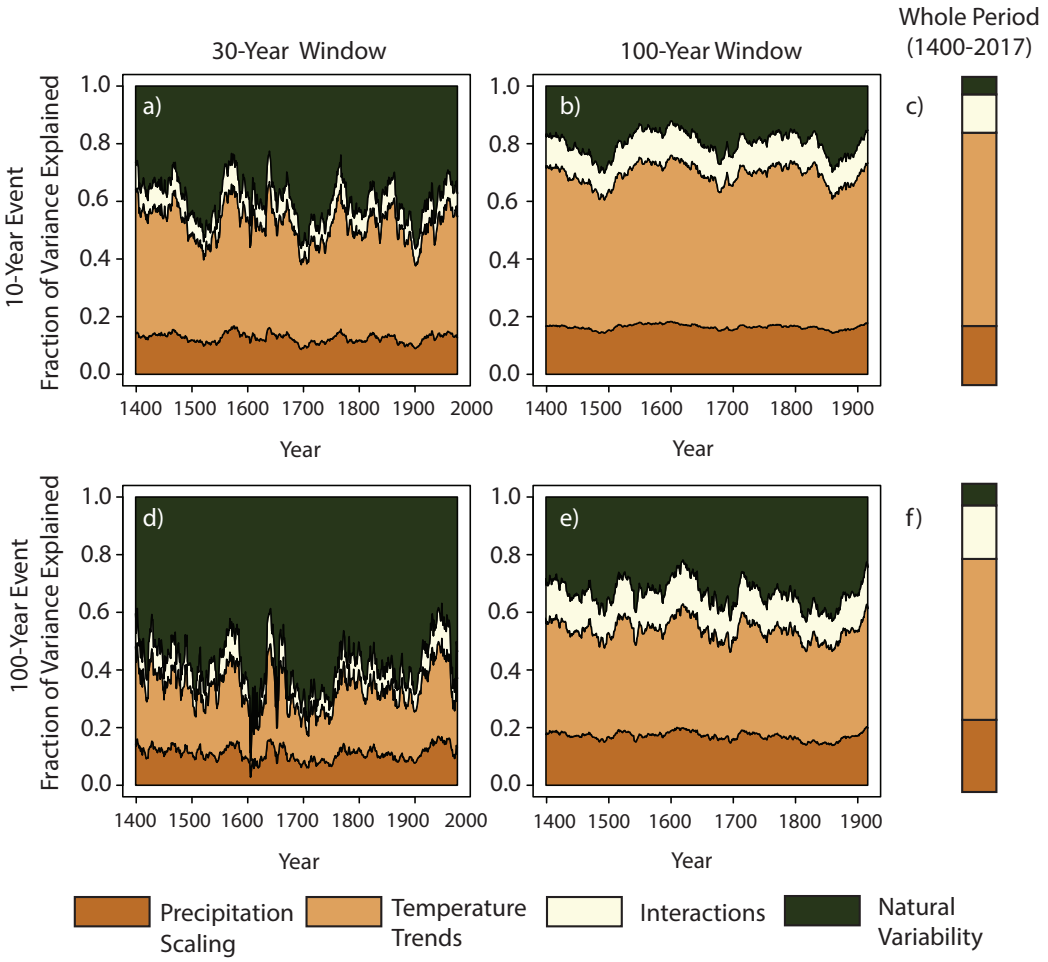

Figure S16. A decomposition of the key drivers of variance in the flood metrics for the New Melones Lake gauge in the Stanislaus River Basin for an a,d) 30-year window b,e) 100-year window and c,f) a 600-year window.

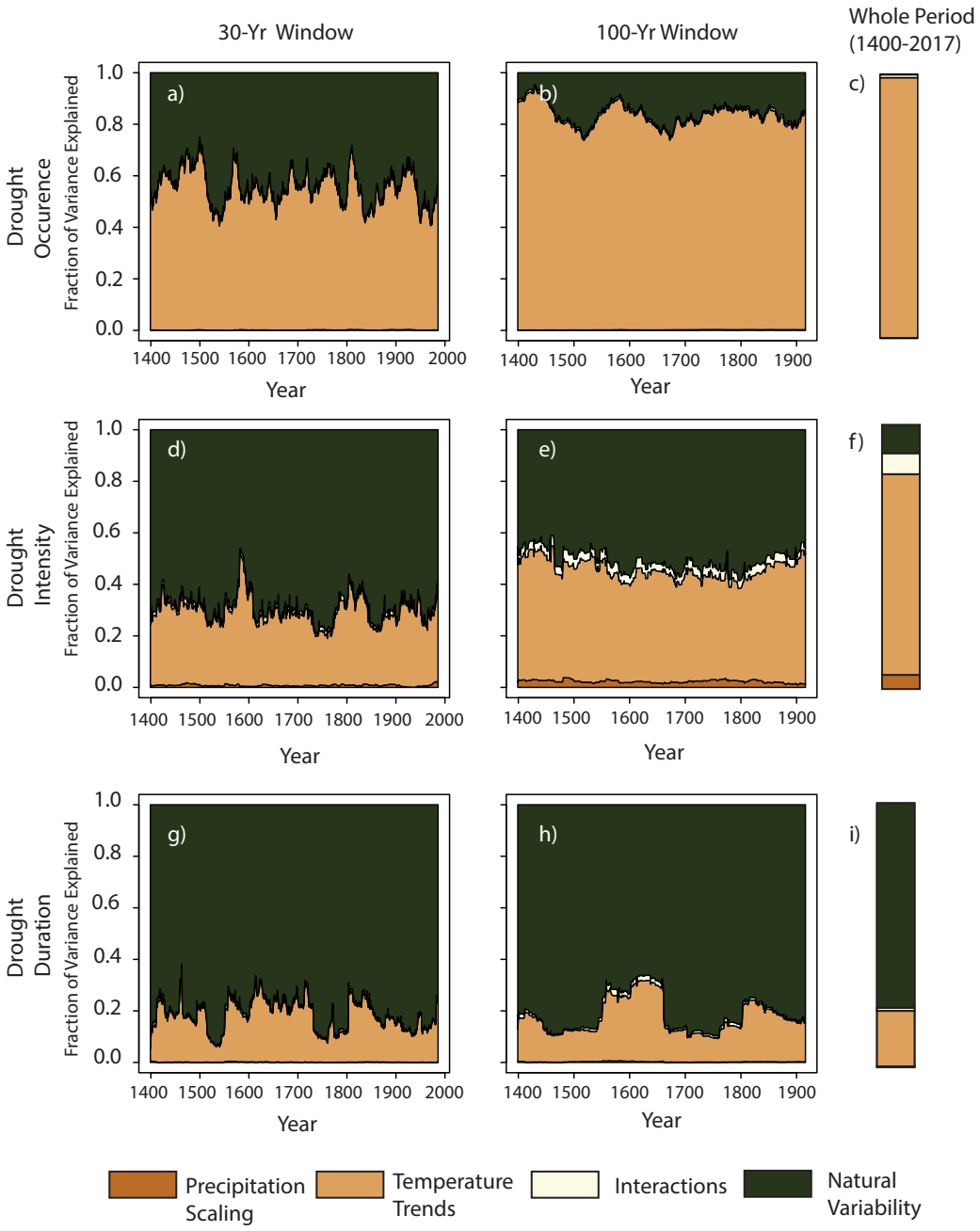

Figure S17. A decomposition of the key drivers of variance in the drought metrics for the Merced Falls gauge in the Merced River Basin for an a,d) 30-year window b,e) 100-year window and c,f) a 600-year window.

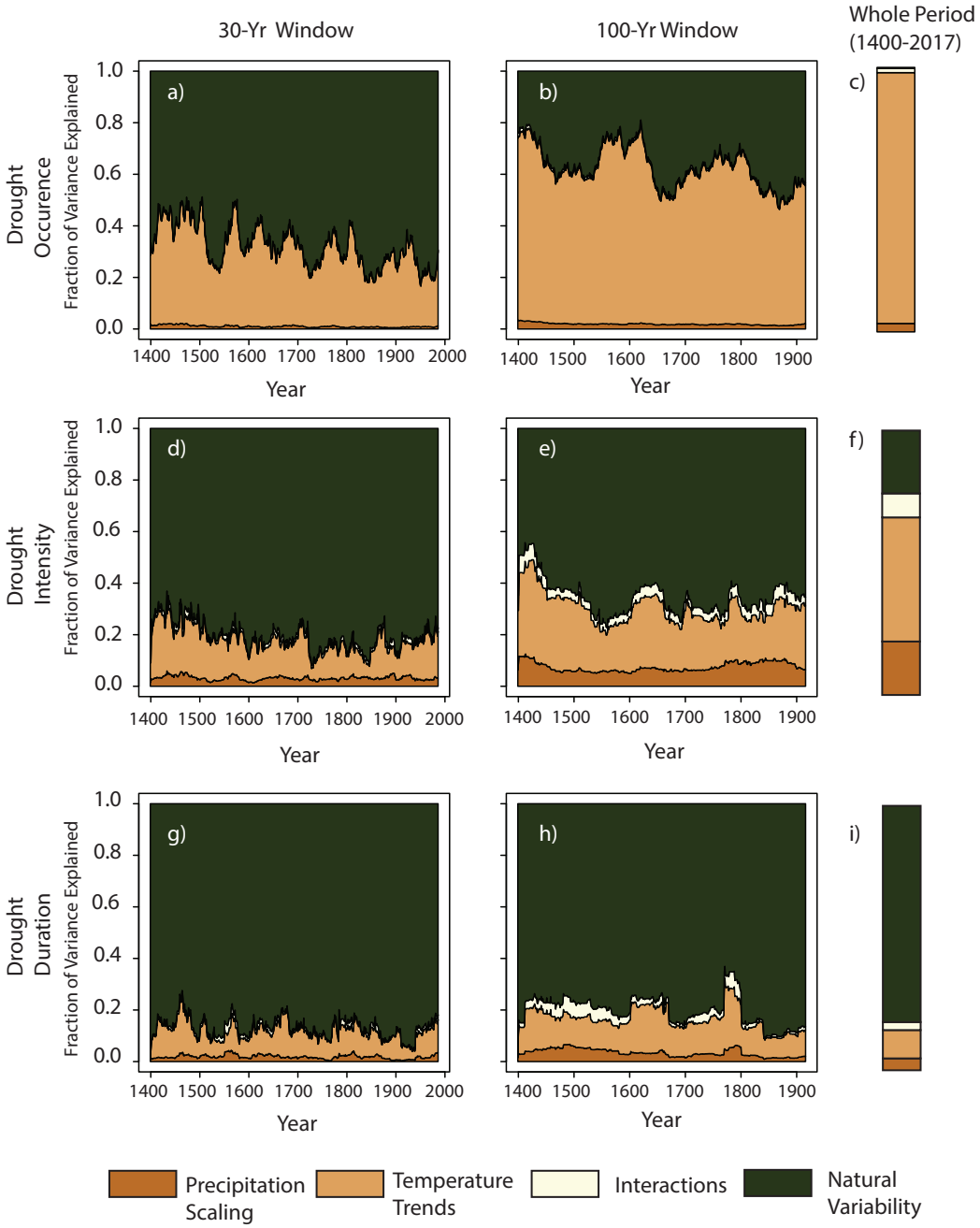

Figure S18. A decomposition of the key drivers of variance in the drought metrics for the Millerton Lake gauge in the San Joaquin Basin for an a,d) 30-year window b,e) 100-year window and c,f) a 600-year window.

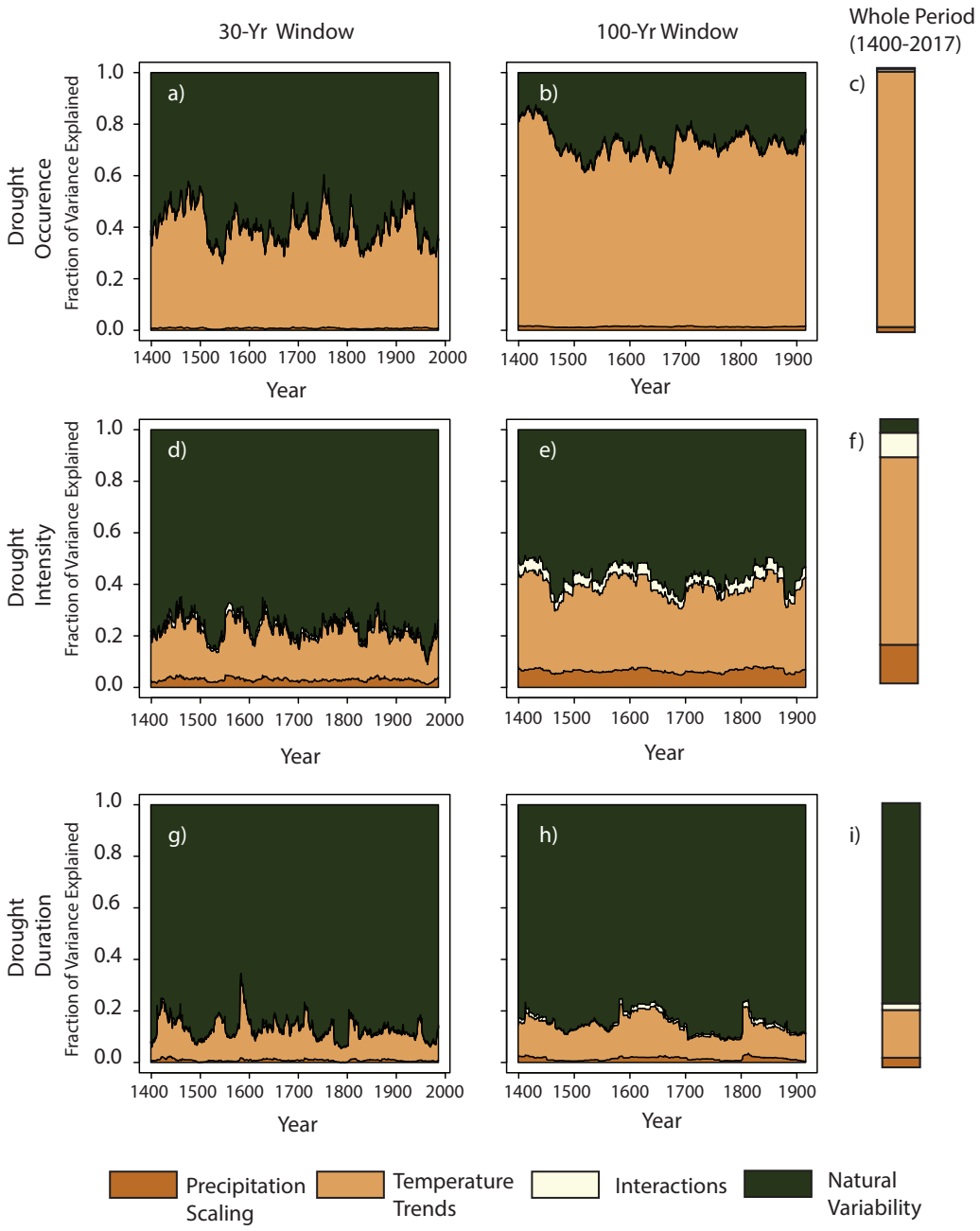

Figure S19. A decomposition of the key drivers of variance in the drought metrics for the New Hogan Lake gauge in the Calaveras River Basin for a,d,g) 30-year window b,e,h) 100-year window and c,f,i) a 600-year window.

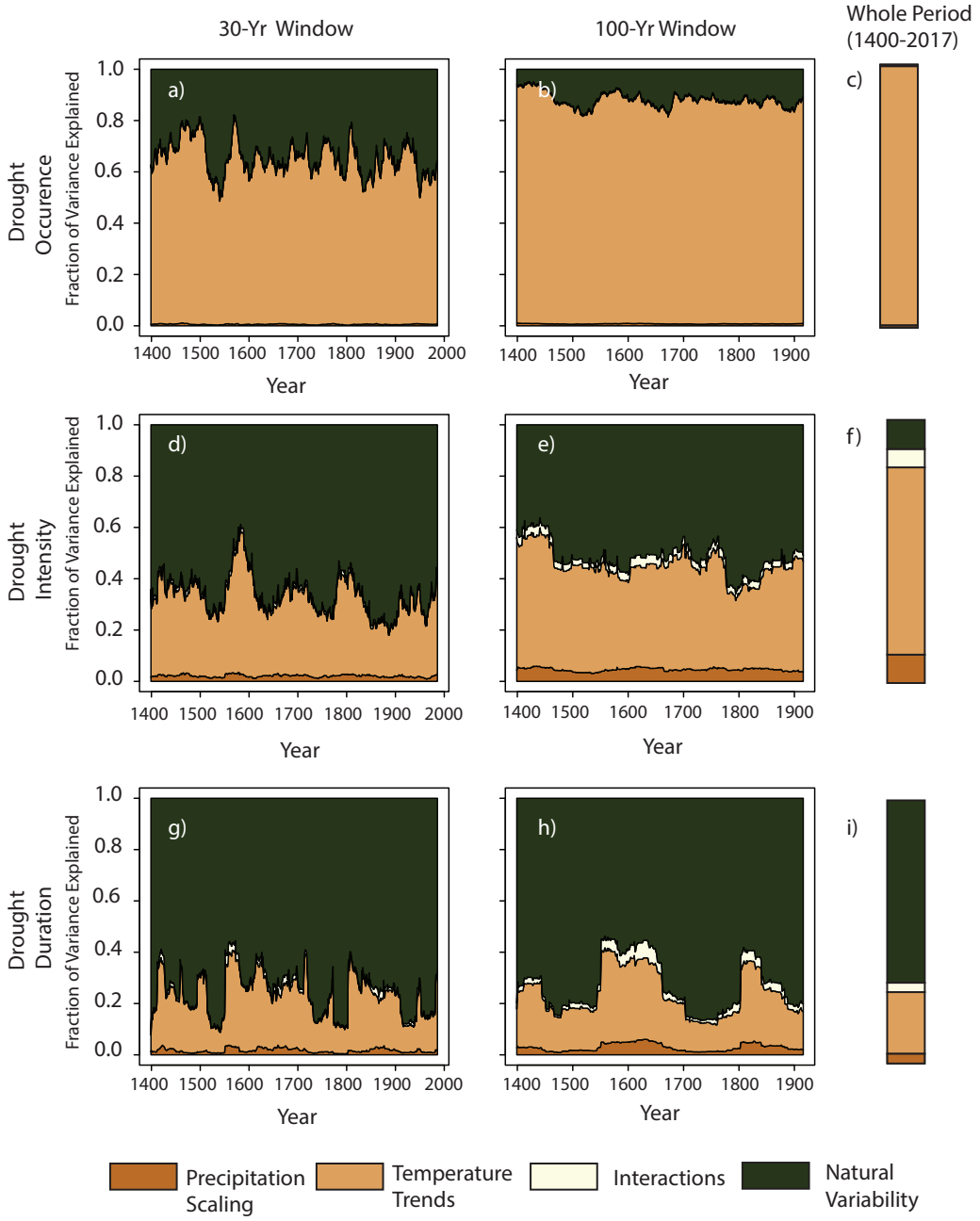

Figure S20. A decomposition of the key drivers of variance in the drought metrics for the New Melones Lake gauge in the Stanislaus River Basin for a,d,g) 30-year window b,e,h) 100-year window and c,f,i) a 600-year window

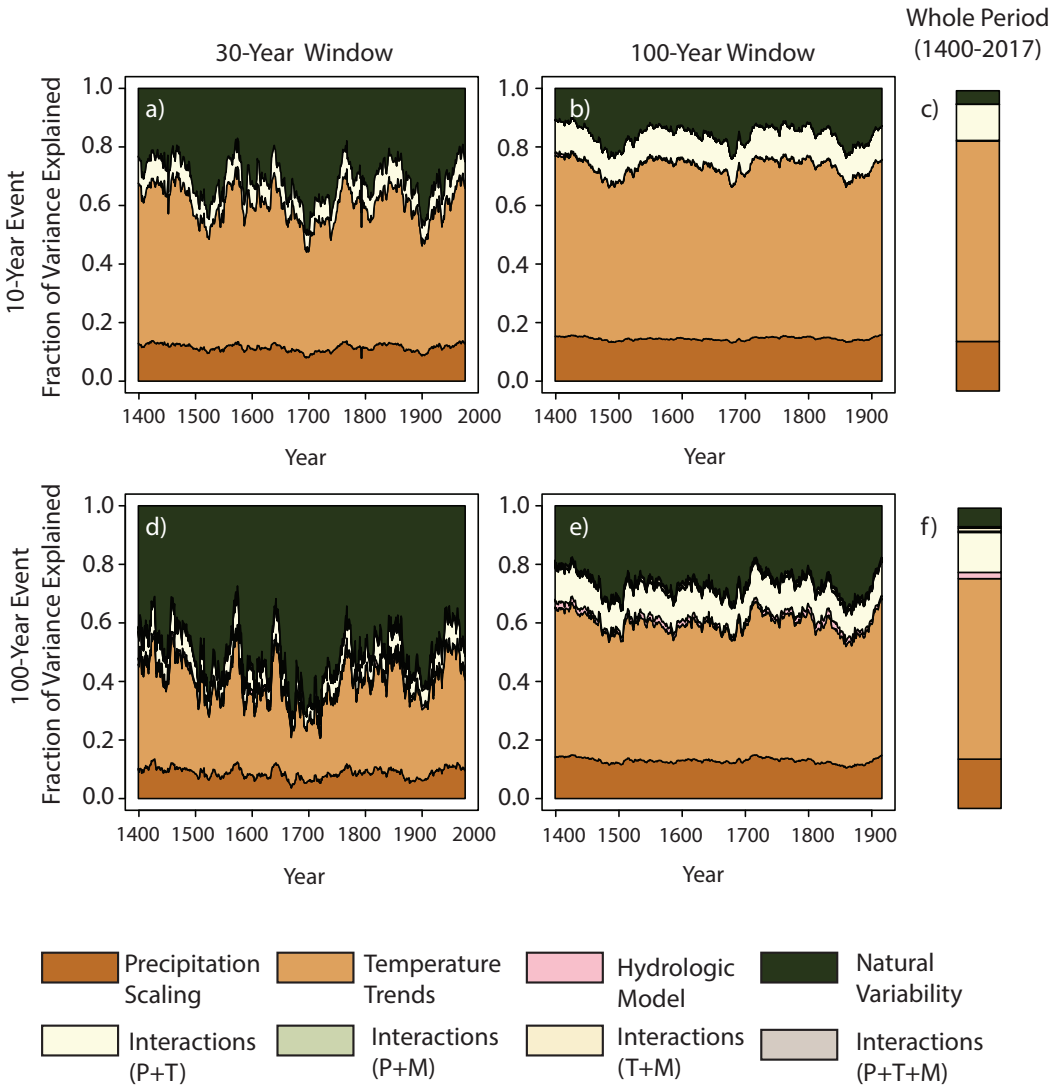

Figure S21. A decomposition of the key drivers of variance in flood metrics for the Tuolumne Basin, with the additional factor of hydrologic model choice.

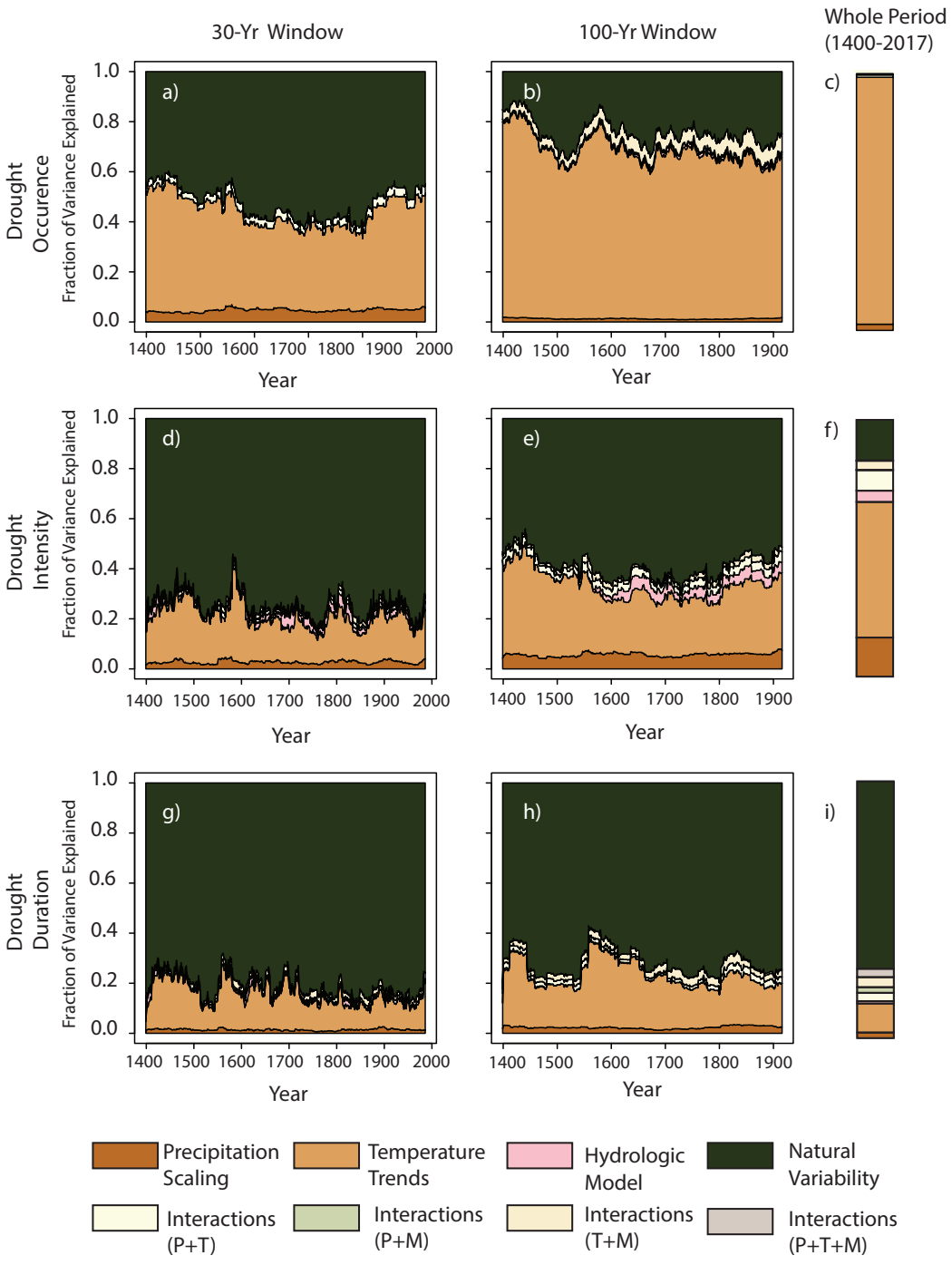

Figure S22. A decomposition of the key drivers of variance in drought metrics for the Tuolumne Basin, with the additional factor of hydrologic model choice.

References

Chegwidden, O. S., Hagen, R., Martin, K., Jones, M., Banihirwe, A., Chiao, C., ... Hamman, J. (2022, October). *Downscaling CMIP6 with multiple statistical methods.* Zenodo. Retrieved from `https://doi.org/10.5281/zenodo.7145491` (The development of this project was funded, in part, through a grant from the Microsoft AI for Earth program to CarbonPlan.) doi: 10.5281/zenodo.7145491

Gupta, R. S., Steinschneider, S., & Reed, P. M. (2022). A multi-objective paleo-informed reconstruction of western us weather regimes over the past 600 years. *Climate Dynamics*, 1–20.

Slivinski, L. C., Compo, G. P., Whitaker, J. S., Sardeshmukh, P. D., Giese, B. S., McColl, C., ... others (2019). Towards a more reliable historical reanalysis: Improvements for version 3 of the twentieth century reanalysis system. *Quarterly Journal of the Royal Meteorological Society*, *145*(724), 2876–2908.

Wi, S., & Steinschneider, S. (2022). Assessing the physical realism of deep learning hydrologic model projections under climate change. *Water Resources Research*, *58*(9), e2022WR032123.